

Current induced magneto-optical Kerr effect as a probe of Dirac carriers in $\text{Bi}_{1-x}\text{Sb}_x$ alloy

Ryota Miyazaki,¹ Shunzhen Wang,¹ Guanxiong Qu,^{2,3} Yukihiro Marui,⁴
Yuta Kobayashi,¹ Masashi Kawaguchi,¹ and Masamitsu Hayashi^{1,5}

¹*Department of Physics, The University of Tokyo, Tokyo 113-0033, Japan*

²*Department of Physics and Astronomy, University of California, Irvine, CA 92697, USA*

³*RIKEN Center for Emergent Matter Science (CEMS), Wako 351-0198, Japan*

⁴*Research Institute of Electrical Communication (RIEC), Tohoku University, Sendai 980-8577, Japan*

⁵*Trans-scale Quantum Science Institute, The University of Tokyo, Tokyo 113-0033, Japan*

(Dated: May 15, 2026)

We study the current-induced magneto-optical Kerr effect (MOKE) in $\text{Bi}_{1-x}\text{Sb}_x$ semi-metallic alloys. The MOKE signal is found to be the largest in pure Bi ($x = 0$), exceeding that of transition metals by nearly four orders of magnitude, and decreases monotonically with increasing Sb concentration. We find the MOKE signal scales with the resistivity (ρ) as $\rho^{1.7 \pm 0.6}$ and with the mobility (μ_c) as $\mu_c^{2.0 \pm 0.2}$. Model calculations show that such exponent can be accounted for if the Dirac electrons are responsible for the generation of spin current. This is in contrast to the ρ^2 and μ_c^{-2} scaling of the MOKE signal induced by the free electrons in parabolic band. The scaling of the MOKE amplitude with the resistivity also partly accounts for the order of magnitude differences of the signal observed between metals, semimetals, and semiconductors. These results demonstrate that current induced MOKE serves as an effective means to characterize the nature of spin current in materials with diverse electronic structures.

The magneto-optical Kerr effect (MOKE) can probe accumulation of spin magnetic moments in semiconductors and metals induced by the spin Hall effect[1–5]. In this approach, current is applied to the sample and the difference in the polarization of the incident and reflected light is measured. The change in the polarization is proportional to the amount of spin magnetic moment that accumulates at the sample edge or surface. To minimize parasitic thermal effects, the applied current density generally must be kept sufficiently low[3, 6, 7]. At such reduced current density, the current-induced MOKE signal in metals is extremely small, typically on the order of a few nanoradians[3, 5, 8]. In contrast, semiconductors exhibit MOKE signals that are several orders of magnitude larger[1]. More recently, MOKE measurements have also been used to detect the accumulation of orbital magnetic moments generated by the orbital Hall effect (OHE)[5, 8–14].

Despite the early discovery of the SHE in semiconductors, the microscopic understanding of the current-induced MOKE signal remains incomplete. In particular, it is not immediately clear why semiconductors with spin Hall angles much smaller than those of metals can produce significantly larger MOKE signals. A recent theoretical model[5] proposed that the MOKE amplitude depends on several material parameters: the spin Hall angle, resistivity, spin diffusion length, and the energy derivative of the ac spin Hall conductivity at the Fermi energy. While this model reproduces the magnitude of the MOKE signal observed in transition metals, its general validity across different material classes remains to be tested.

Here we investigate the current-induced MOKE in semimetallic $\text{Bi}_{1-x}\text{Sb}_x$ alloy thin films to address these questions. Although $\text{Bi}_{1-x}\text{Sb}_x$ is known to host a topo-

logical insulator phase in the Bi-rich regime [15–18], we focus on its bulk semi-metallic character by using relatively thick films[19–22]. The transport properties and the MOKE signal are studied as a function of $\text{Bi}_{1-x}\text{Sb}_x$ composition. We find the MOKE signal scales with the resistivity, carrier density and mobility, which can be accounted for with the model.

$\text{Bi}_{1-x}\text{Sb}_x$ thin films were grown on quartz (SiO_2) and Si substrates. We used the films on quartz substrate to measure the current-induced MOKE and the transport properties. XRD and ellipsometry measurements were performed using the films on Si substrate. A 1 nm-thick Ta seed layer was first deposited on the substrate using RF magnetron sputtering to promote smooth growth of $\text{Bi}_{1-x}\text{Sb}_x$. Since the seed layer is predominantly amorphous, we assume the structure of the film is similar for films deposited on quartz and Si substrates. $\text{Bi}_{1-x}\text{Sb}_x$ was then formed using molecular beam epitaxy (MBE) at ambient substrate temperature. Bi and Sb were co-evaporated to form the alloy. The temperature of the Knudsen cells was adjusted to tune the deposition rates of Bi and Sb, which define the composition of the film. The thickness of $\text{Bi}_{1-x}\text{Sb}_x$ was set close to 60 nm, significantly larger than the penetration depth of the light (wavelength: 633 nm) used in the experiments. Finally, a 1 nm-thick Ti capping layer was deposited by electron-beam evaporation to prevent oxidation of the film.

Hall bars were made by mechanically scratching the films. See Fig. 1 for a sketch of the device. The width of the current channel of the Hall bars is $\sim 400 \mu\text{m}$. Electrodes to the Hall bars, made of 2 Ta/10 Al/3 Pt (thickness in nm), were formed using a standard lift-off process. The transport properties of the films were characterized using four point probe and Hall resistance measurements.

Figure 2(a) shows the film resistivity $\bar{\rho}_{xx}$ as a function

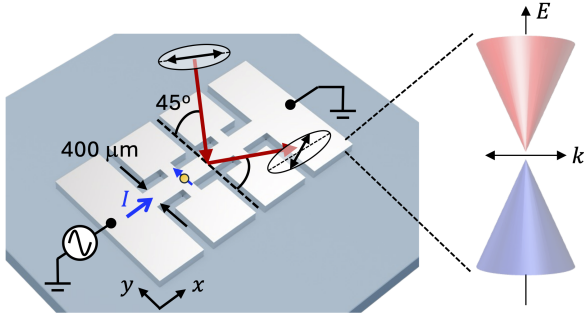


FIG. 1. Schematic illustration of the Hall bar, the incident and reflected light, and definition of the coordinate system. As current is passed along the Hall bar, spin Hall effect of $\text{Bi}_{1-x}\text{Sb}_x$ induces spin accumulation at the film surface, which is detected by a change in the polarization between the incident and reflected light. The sample is composed of Bi-rich $\text{Bi}_{1-x}\text{Sb}_x$, which possess a linear Dirac-like dispersion, as sketched on the right, near the L -point in the Brillouin zone. We show the MOKE signal probes the Dirac-like dispersion at the Fermi level.

of Sb concentration x . $\bar{\rho}_{xx}$ is obtained by the measured film resistance, the width and length of the Hall bar and the total thickness of the conducting layers (1 nm-thick Ta and 60 nm-thick $\text{Bi}_{1-x}\text{Sb}_x$). Here the difference in the resistivity of the Ta seed and $\text{Bi}_{1-x}\text{Sb}_x$ layers is neglected. Current flow in the 1 nm-thick Ti capping layer, which is heavily oxidized, is neglected. Overall, $\bar{\rho}_{xx}$ tends to decrease with increasing x . Pure Bi has the largest $\bar{\rho}_{xx}$ which exceeds 2000 $\mu\Omega\text{cm}$. We use a two carrier model, with equal electron and hole mobilities, to extract the carrier density and mobility from the out of plane magnetic field dependence of the longitudinal and transverse resistances[23, 24]. The x dependence of the carrier density n_c (the sum of electron and hole densities) and the mobility μ_c are plotted in Figs. 2(b) and 2(c), respectively. n_c increases exponentially with x . In contrast, μ_c linearly decreases with x . These trends are consistent with previous reports on $\text{Bi}_{1-x}\text{Sb}_x$ [23, 25, 26]. The change in the resistivity with x is thus primarily caused by the change in n_c .

Schematic illustration of the MOKE measurement setup[5] is shown in Fig. 3(a). A HeNe laser with a wavelength of 633 nm is used as the light source. The beam passes through a band-pass filter and a polarizer to create a linear polarization, and is then directed to the sample from an oblique angle ($\sim 45^\circ$ from the film normal). The diameter of the laser spot at the sample surface is $\sim 25 \mu\text{m}$. The reflected light moves through a half-wave plate (HWP) or combination of a HWP and a quarter-wave plate (QWP) and is split by a polarized beam splitter into two orthogonally polarized components. These components are detected simultaneously by a balanced photodetector and subsequently converted into electrical signals. The signal is fed into a lock-in amplifier synchronized with the frequency ($\sim 2 \text{ kHz}$) and phase of

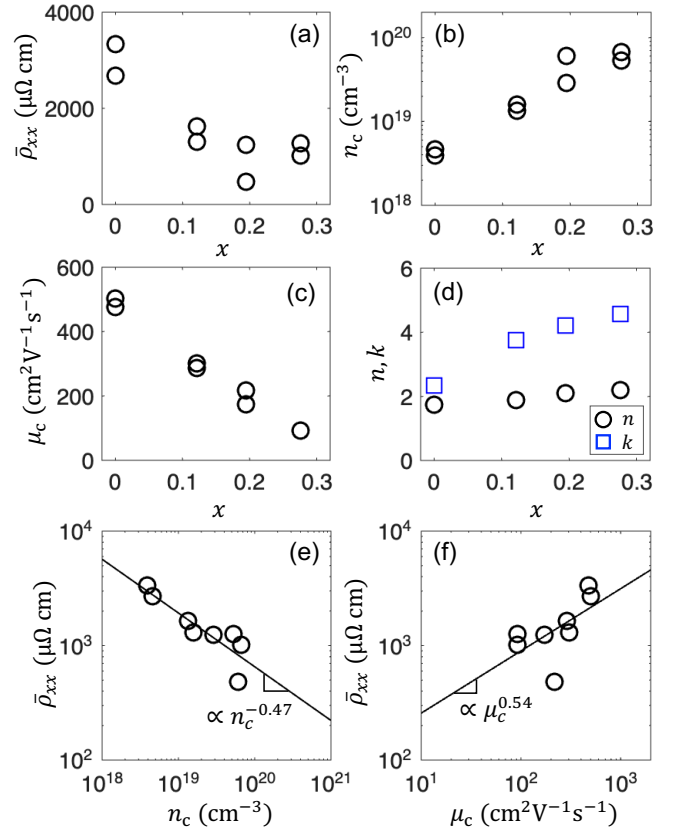


FIG. 2. Sb concentration x dependence of the resistivity $\bar{\rho}_{xx}$ (a) carrier density n_c (b), mobility μ_c (c), the refractive index n and the extinction coefficient k (d) of the $\text{Bi}_{1-x}\text{Sb}_x$ thin films. (a-c) Data from two devices on the same substrates are presented. (e,f) n_c (e) and μ_c (f) dependence of $\bar{\rho}_{xx}$ plotted for all films. The solid lines show linear fit to the log-log plot.

the ac current applied to the sample. The real part of the MOKE signal (θ_K , rotation angle) and the imaginary part (η_K , ellipticity angle) were measured using the HWP and HWP/QWP, respectively. Positive θ_K and η_K is defined as the polarization and elliptical angle of the reflected light rotating clockwise when seen from the sample side. We vary the ac current amplitude and measure the MOKE signal. Positive and negative currents indicate ac current that are 180 deg out of phase to each other. This process is repeated N times ($N \sim 10 - 100$) to increase the signal to noise ratio. All measurements were performed at room temperature.

Figures 3(b) and 3(c) show representative current density (j) dependence of θ_K and η_K for $\text{Bi}_{1-x}\text{Sb}_x$ with $x = 0$ (pure Bi). The current that flows through the film is determined by measuring the voltage across a standard resistor connected in series with the Hall bar. The current density j in $\text{Bi}_{1-x}\text{Sb}_x$ is estimated by assuming a parallel circuit in which current flows through the two conducting layers, 1 nm-thick Ta and 60 nm-thick $\text{Bi}_{1-x}\text{Sb}_x$. The resistivity of Ta (ρ_{Ta}) is assumed to be $\sim 200 \mu\Omega\text{cm}$, ob-

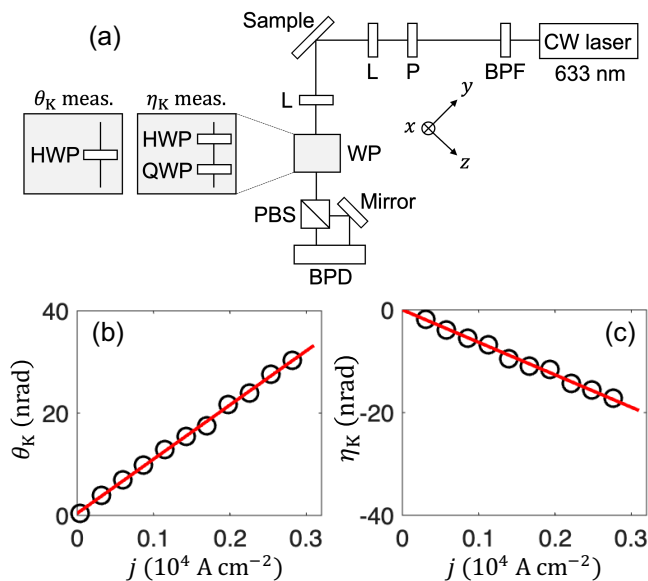


FIG. 3. (a) Schematic illustration of the measurement setup and definition of the coordinate system. The incident light is *s*-polarized (polarization is along the *x*-axis). BPF: bandpass filter, P: polarizer, L: lens, HWP: half-wave plate, QWP: quarter-wave plate, PBS: polarized beam splitter, BPD: balanced photodetector. (b,c) Current density *j* dependence of the real part θ_K (b) and the imaginary part η_K (c) of the MOKE signal for pure Bi ($x = 0$). The red solid lines show linear fit to the data.

tained from experiments on similar systems[27]. We also estimate the resistivity of $\text{Bi}_{1-x}\text{Sb}_x$, defined as ρ_{xx} , from the film resistivity $\bar{\rho}_{xx}$, ρ_{Ta} and the layer thicknesses, using the parallel circuit model. Both θ_K and η_K linearly increase with *j*, suggesting that effects due to current-induced heating is negligible. We fit the data with a linear function to extract the rate at which the MOKE signal changes with *j*, i.e. θ_K/j and η_K/j . The magnitude of the MOKE signal, $|\theta_K + i\eta_K|/j$ is plotted against *x* in Fig. 4(a), black circles. As is evident, the magnitude of the MOKE signal monotonically decreases with *x* in log scale.

A phenomenological model was previously developed[5] to account for the MOKE signal. According to this model, θ_K and η_K are expressed as the following:

$$\theta_K + i\eta_K = -\frac{ie}{\varepsilon_0\omega} \left. \frac{\partial \sigma_s(\omega)}{\partial E} \right|_{E_F} l_s \sigma_s(0) \rho_{xx}^2 j h(\varepsilon_{xx}, \theta, t, l_s). \quad (1)$$

$\sigma_s(0)$ and l_s are the dc spin Hall conductivity and the spin diffusion length, respectively. $\sigma_s(\omega)$ is the ac spin Hall conductivity driven by the light electric field with angular frequency ω . $\partial \sigma_s(\omega)/\partial E|_{E_F}$ is the energy derivative of $\sigma_s(\omega)$ evaluated at the Fermi energy E_F . $\partial \sigma_s(\omega)/\partial E|_{E_F}$ is equivalent to the derivative of the transverse conductivity with (spin dependent) carrier density, where the

latter is known to represent inter-band transitions[5]. $h(\varepsilon_{xx}, \theta, t, l_s)$ is a complex function of the diagonal component of the permittivity tensor ε_{xx} , the angle θ between the incident light wave vector and the film normal, film thickness *t* and l_s . See Appendix, Sec. IC for the exact form of $h(\varepsilon_{xx}, \theta, t, l_s)$. ε_0 and *e* are the vacuum permittivity and the electric charge, respectively.

First, we show that Eq. (1) provides order of magnitude estimates of the MOKE signal that are consistent with the experiments. Here we neglect contribution from the orbital Hall effect for simplicity: see Appendix, Sec. IC, for the calculation results when the orbital Hall effect is considered. The Maxwell's equations are solved numerically[28–30] to compute $h(\varepsilon_{xx}, \theta, t, l_s)$ [5]. The dc and ac spin Hall conductivities are obtained from tight binding model calculations of the electronic structure of $\text{Bi}_{1-x}\text{Sb}_x$ and the Kubo formula[22, 31, 32]. The *x*-dependence of $\sigma_s(0)$ and $\partial \sigma_s(\omega)/\partial E|_{E_F}$ are shown in the Appendix, Fig. 7(d-f). $\sigma_s(0)$ is nearly constant in the range of *x* shown here, consistent with previous calculations[32]. Values of ρ_{xx} extracted from the film resistivity $\bar{\rho}_{xx}$ are shown in the Appendix, Table III. Here we take the average of ρ_{xx} obtained from two devices for a given *x*. ε_{xx} is determined by the refractive index *n* and the extinction coefficient *k*, obtained using standard ellipsometry measurements. The *x* dependence of *n* and *k* are shown in Fig. 2(d). *n* and *k* tend to increase with increasing *x*. l_s for Bi (~ 18 nm) was estimated previously[33]. We set $l_s \sim 18$ nm for all films. Such assumption is consistent with Dyakonov-Perel (DP)-type spin relaxation, where l_s shows little dependence on the resistivity: see the discussion pertaining to Eq. (5) for the details.

The purple squares in Fig. 4(a) show the *x* dependence of the calculated MOKE signal ($|\theta_K + i\eta_K|/j$) using Eq. (1). As is evident, the calculation roughly reproduces the trend of the MOKE signal as a function of *x*. Whereas the calculated results are close to that of the experiments for $x = 0$, the former is overall smaller than that of the latter when $x > 0$. Including the contribution from the orbital Hall effect mitigates the difference: see Appendix, Sec. IC. It is also possible that the topological surface states, which is not included in the model calculations, contribute to the MOKE signal when $0.09 \lesssim x \lesssim 0.22$ [32].

Next, we study the relations between the transport properties and the MOKE signal to further test the validity of Eq. (1). In Fig. 4(b-d), we show $|\theta_K + i\eta_K|/j$ plotted against ρ_{xx} , n_c and μ_c using a log-log plot. $|\theta_K + i\eta_K|/j$ scales with ρ_{xx} , n_c and μ_c . The log-log plot is fitted with a linear function to obtain the exponent of the scaling relations. The fitting results, shown by the black solid lines, agree well with the data. In Fig. 4(b), data for $\text{In}_{0.07}\text{Ga}_{0.93}\text{As}$, Pt, V, extracted from Refs. [1] and [5], are presented together. Overall, we find that the difference in the MOKE signal can be roughly accounted for with the difference in ρ_{xx} . In the following, we compare the exponents obtained from the fitting with those pre-

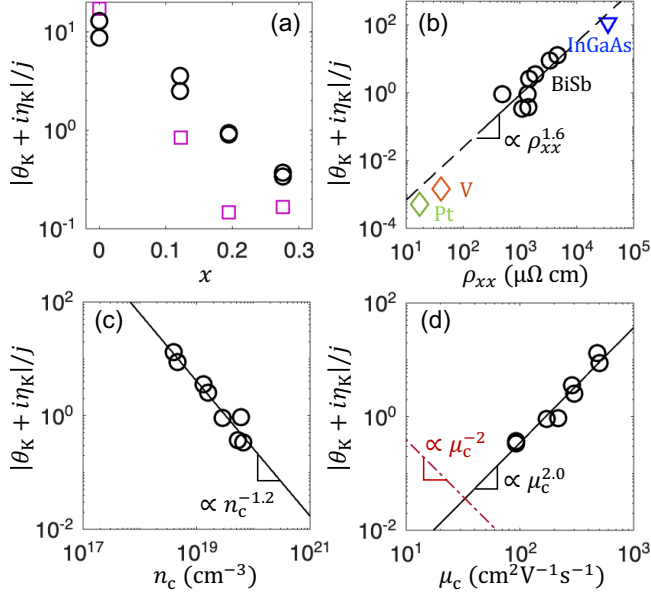


FIG. 4. (a) Black circles: Sb concentration x dependence of the magnitude of the MOKE signal per unit current density $|\theta_K + i\eta_K|/j$. Purple squares: calculated signal based on Eq. (1). Contribution from the orbital Hall effect is neglected. (b-d) Black circles: $|\theta_K + i\eta_K|/j$ of $\text{Bi}_{1-x}\text{Sb}_x$ (BiSb) plotted against the resistivity ρ_{xx} (b), carrier density n_c (c) and mobility μ_c (d). The orange, green diamonds and the blue triangle in (b) show data for V, Pt[5] and $\text{In}_{0.07}\text{Ga}_{0.93}\text{As}$ [1], respectively. The black solid lines in (b-d) indicate fit to the data of $\text{Bi}_{1-x}\text{Sb}_x$. The red dashed-dotted line in (d) show calculation result assuming a parabolic free electron model with the intrinsic spin Hall effect and DP-type spin relaxation. (a-d) The unit of the y -axis is 10^{-3} nrad cm^2/A .

dicted by Eq. (1).

As some of the parameters in Eq. (1) are implicitly dependent on ρ_{xx} , n_c , μ_c , here we clarify the relations. For this purpose, it is convenient to introduce the relaxation time τ_{eff} which determines the carrier transport properties. Let us assume that τ_{eff} satisfies the following general relation[21, 34, 35]

$$\tau_{\text{eff}} = a_0 n_c^\alpha, \quad (2)$$

where a_0 and α are constants. Previous studies reported that α depends on the electronic structure of the host material. For example, $\alpha = -\frac{1}{3}$ when the band structure is described by the Dirac Hamiltonian[21, 35] (we refer to electrons in such system as Dirac electrons). For free electrons in a parabolic band, $\alpha = 0$ is often adopted. Bichir $\text{Bi}_{1-x}\text{Sb}_x$ alloys used in this study belong to the former: the carriers near the L point of the Brillouin zone at the Fermi level are categorized as Dirac electrons[23, 32]. Although we cannot distinguish effects from topological surface states[15–18, 36, 37], if any, for simplicity here we focus on spin transport properties that originate from the bulk states and thus compare model calculation results

assuming Dirac electrons and free electrons. The value of α for the Dirac model is determined using the experimental results presented in Fig. 2, while we fix $\alpha = 0$ for the free electron model.

In Fig. 2(e,f), we show the relation between ρ_{xx} and n_c , μ_c . The resistivity decreases with increasing n_c , however, it increases with increasing μ_c . This is in stark contrast with metals, where ρ_{xx} typically decreases with increasing μ_c . As we show below, these scalings reflect the character of Dirac electron system. We fit the log-log plot in Fig. 2(e,f) with a linear line to obtain the scaling exponents. To obtain the scaling relation, we first express $\rho_{xx} = (n_c e \mu_c)^{-1}$ in terms of τ_{eff} . For Dirac electrons, μ_c possesses a unique relation with n_c [21], which reads

$$\mu_c = a_1 n_c^{\alpha-1/3}, \quad (3)$$

where a_1 is a constant. The mobility of the Dirac and free electron systems is therefore given by

$$\mu_c = \begin{cases} \left(a_1 a_0^{-1+\frac{1}{3\alpha}} \right) \tau_{\text{eff}}^{1-\frac{1}{3\alpha}} : \text{Dirac}, \\ \left(\frac{e}{m_{\text{eff}}} \right) \tau_{\text{eff}} : \text{Free}, \end{cases} \quad (4)$$

where the former is derived from Eqs. (2) and (3), and the latter is based on the Drude model. Substituting Eqs. (2) and (4) into $\rho_{xx} = (n_c e \mu_c)^{-1}$, we obtain the scaling relations between ρ_{xx} and τ_{eff} , from which we find the relations between ρ_{xx} and n_c , μ_c . The relations are summarized in Table I. For the free electron model, the exponents are all -1, consistent with the Drude model. The exponents derived from the Dirac model depends on α . For example, if we substitute $\alpha = -\frac{1}{3}$, we find $\rho_{xx} \propto n_c^{-1}$ and $\rho_{xx} \propto \mu_c^{\frac{1}{2}}$. As noted above, in the Dirac model, ρ_{xx} increases with increasing μ_c .

In Table I, the exponents obtained from the experiments are presented in the bottom row. We equate these exponents with the form from the Dirac model to determine α : we find $\alpha \sim -0.20$ and $\alpha \sim -0.32$ from the scaling of ρ_{xx} with n_c and μ_c , respectively. These values are close to what the theory predicts for the Dirac electrons: $\alpha = -\frac{1}{3}$ [35]. For the Dirac model, we therefore assume that α lies in between -0.20 and -0.32 .

We now examine the relation between the MOKE amplitude $|\theta_K + i\eta_K|$ and n_c , μ_c , ρ_{xx} based on Eq. (1). In doing so, we must determine how l_s and σ_s depend on τ_{eff} . The spin diffusion length is given by $l_s = \sqrt{D\tau_s}$, where the diffusion constant D for the Dirac electrons[38] and

TABLE I. Values of the exponent ν for the scaling relations $\rho_{xx} \propto \tau_{\text{eff}}^\nu$, $\rho_{xx} \propto n_c^\nu$ and $\rho_{xx} \propto \mu_c^\nu$.

model	τ_{eff}^ν	n_c^ν	μ_c^ν
Dirac	$-1 - \frac{2}{3\alpha}$	$-\alpha - \frac{2}{3}$	$-\frac{3\alpha+2}{3\alpha-1}$
Free	-1	-1	-1
Exp.	n/a	-0.47	0.54

the free electrons are given by

$$D = \begin{cases} \frac{1}{3} v_F^2 \tau_{\text{eff}} : \text{ Dirac,} \\ \frac{E_F}{e} \mu_c = \frac{E_F}{m_{\text{eff}}} \tau_{\text{eff}} : \text{ Free.} \end{cases} \quad (5)$$

v_F is the Fermi velocity and m_{eff} is the effective mass. For the free electrons, we used the Einstein relation and Eq. (4). τ_s is the spin relaxation time, given by

$$\tau_s = a_2 \tau_{\text{eff}}^\delta, \quad (6)$$

where a_2 is a constant, $\delta = -1$ [1] for the Dyakonov-Perel (DP) [Elliott-Yafet (EY)]-type spin relaxation. For the dc spin Hall conductivity $\sigma_s(0)$, we consider two contributions, intrinsic and extrinsic (skew scattering). It is common to assume

$$\sigma_s(0) = a_3 \tau_{\text{eff}}^\beta. \quad (7)$$

where a_3 is a constant. $\beta = 0$ for the intrinsic SHE and $\beta = 1$ for the extrinsic SHE (skew scattering). Note that such relation and those shown in Table I return $\rho_s(0) \propto \rho_{xx}^{-\beta+2}$ for the free electron model, where $\rho_s(0)$ is the dc spin Hall resistivity. The scaling between $\rho_s(0)$ and ρ_{xx} has been used to determine the origin of the spin Hall effect in metals[39, 40]. We assume the ac spin Hall conductivity $\sigma_s(\omega)$ is not dependent on τ_{eff} as the relaxation time is typically significantly larger than the period of the light electric field. For example, in pure Bi, $\tau_{\text{eff}} \sim 10^{-12} - 10^{-11}$ s[21], whereas the period of the light is 2×10^{-15} s. With these relations, the variation of $|\theta_K + i\eta_K|$ with n_c , μ_c and ρ_{xx} can be derived, which are summarized in Table II.

We calculate the exponents presented in Table II by substituting the appropriate values of α , β and δ . For the free electron model with an intrinsic SHE and a DP-type spin relaxation, we find $|\theta_K + i\eta_K| \propto n_c^0$, $|\theta_K + i\eta_K| \propto \rho_{xx}^2$ and $|\theta_K + i\eta_K| \propto \mu_c^{-2}$. The last relation is drawn by the red dash-dotted line in Fig. 4(d) for reference. The scaling between $|\theta_K + i\eta_K|$ and ρ_{xx} roughly agrees with the trend found in the experiments. However, the scaling relation of $|\theta_K + i\eta_K|$ with μ_c is clearly inconsistent with the experimental results of $\text{Bi}_{1-x}\text{Sb}_x$.

To illustrate how the scaling relations differ between the Dirac and free electron models in more detail, we show the calculated exponents for $|\theta_K + i\eta_K|$ vs. n_c , μ_c and ρ_{xx} in Fig. 5(a,b) [Dirac electrons] and 5(c,d) [free electrons]. Figure 5(a,c) [(b,d)] show the results when the intrinsic (extrinsic) SHE is considered. The red and blue

TABLE II. Forms of the exponent ν for the scaling relations $|\theta_K + i\eta_K| \propto \tau_{\text{eff}}^\nu$, $|\theta_K + i\eta_K| \propto n_c^\nu$, $|\theta_K + i\eta_K| \propto \mu_c^\nu$ and $|\theta_K + i\eta_K| \propto \rho_{xx}^\nu$. $A \equiv \beta + \frac{1}{2}(1 + \delta) - 2\frac{3\alpha+2}{3\alpha}$ and $B \equiv \beta + \frac{1}{2}(1 + \delta) - 2$.

model	τ_{eff}^ν	n_c^ν	μ_c^ν	ρ_{xx}^ν
Dirac	A	αA	$\frac{3\alpha}{3\alpha-1} A$	$-\frac{3\alpha}{3\alpha+2} A$
Free	B	0	B	$-B$

bars represent results when the DP-type and EY-type spin relaxations are assumed. The range of the colored vertical bars for the Dirac electrons [Fig. 5(a,b)] indicate variation of the exponents when α is varied from -0.32 to -0.2. For the free electron model, α is fixed to 0, thus the symbol is a single line. The exponents obtained from the experiments (Fig. 4) are shown using the open circles. We find that the Dirac model describes the experimental results of $\text{Bi}_{1-x}\text{Sb}_x$ better than the free electron model. This is primarily because the experiments dictate the exponents of $|\theta_K + i\eta_K|$ vs. μ_c and ρ_{xx} have the same sign, which is not the case for the free electron model. From the comparison presented in Fig. 5, it is difficult to determine the origin of the SHE (intrinsic vs. extrinsic) or the spin relaxation mechanism (DP vs. EY). The calculation results do not significantly change if one assumes the ac spin Hall conductivity to be an extrinsic origin, i.e. $\sigma_s(\omega) \propto \tau_{\text{eff}}$. Recent studies have reported an unconventional scaling of the orbital Hall conductivity $\sigma_o(0)$ with the resistivity, that is, assuming a free electron model, $\sigma_o(0) \propto \rho_{xx} \propto \tau_{\text{eff}}^{-1}$ [41]. However, we find such scaling cannot account for the experimental results.

These results therefore show that the model developed to describe current induced MOKE in metals can also account for the results from semi-metallic $\text{Bi}_{1-x}\text{Sb}_x$. Moreover, the MOKE signal scales with the transport parameters that reflect the Dirac-like band structure of $\text{Bi}_{1-x}\text{Sb}_x$ [16, 21, 32, 42–44]. Finally, recent studies have suggested that the current induced MOKE signal may contain contribution from electro-optic effects[45–48]. We find that the MOKE signal does not change its sign when we change the incident light polarization

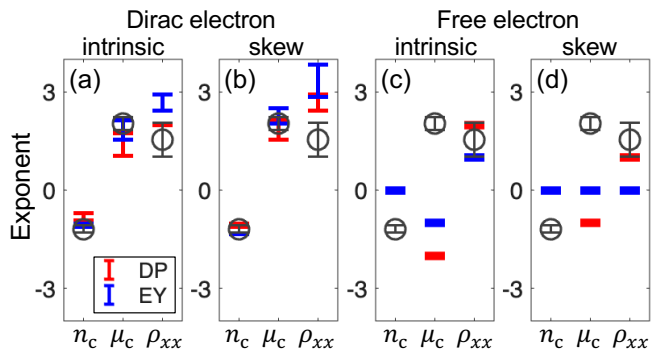


FIG. 5. (a-d) Values of the exponent ν for the scaling relations $|\theta_K + i\eta_K| \propto n_c^\nu$ (left), μ_c^ν (center) and ρ_{xx}^ν (right). The open circles display the ν obtained in the experiments. The attached black error bars represent the fitting error when a linear function is fitted to the log-log plot shown in Fig. 4(b-d). The horizontal colored bars shows the ν estimated using the Dirac model (a,b) and the free electron model (c,d) with DP (red bars, $\delta = -1$) and EY (blue bars, $\delta = 1$) spin relaxations. (a,c) and (b,d) show results with the intrinsic ($\beta = 0$) and extrinsic ($\beta = 1$) SHE. The range of the horizontal bar for the Dirac model represents calculation results with $-0.32 \leq \alpha \leq -0.20$. $\alpha = 0$ for the free electron model.

from s to p , which indicates that contribution from the intrinsic electro-optic effect is small[47]. Further studies are required to clarify the contributions from the extrinsic electro-optic effect (e.g. current induced orbital Kerr effect)[49].

In summary, we have investigated the current-induced MOKE in semi-metallic $\text{Bi}_{1-x}\text{Sb}_x$ alloy thin films. The MOKE signal increases with decreasing Sb concentration, reaching its maximum in pure Bi ($x = 0$), where it exceeds that of typical transition metals by nearly four orders of magnitude. The signal scales with the resistivity as $\rho_{xx}^{1.7 \pm 0.6}$ and with the carrier mobility as $\mu_c^{2.0 \pm 0.2}$. These scaling relations are consistent with model calculations that assume the Dirac electrons are responsible for the generation and accumulation of spin magnetic moment, in contrast to the ρ_{xx}^2 and μ_c^{-2} scaling predicted by the parabolic free electron model. Although the scaling exponent of MOKE with resistivity is different between the free electron-like transition metals and the Dirac semimetals, the scaling with ρ_{xx} can mostly account for the order of magnitude differences found among metals, semi-metals and semiconductors. These results thus demonstrate that current-induced MOKE serves as a sensitive probe of spin current and the underlying electronic state in a broad class of materials.

ACKNOWLEDGMENTS

We thank ARIM for the support on the ellipsometry measurements. This work was partly supported by JSPS KAKENHI (Grant Number 23H00176), JST CREST (JPMJCR19T3), MEXT Initiative to Establish Next-generation Novel Integrated Circuits Centers (X-NICS) and Cooperative Research Project Program of RIEC, Tohoku University. R.M. thanks Support Center for Advanced Telecommunications Technology Research (SCAT) and S.W. thanks JST SPRING GX, Grant Number JPMJSP2108.

I. APPENDIX

A. Transport properties

In Table III, we show the estimated resistivity of $\text{Bi}_{1-x}\text{Sb}_x$ (ρ_{xx}) using the parallel circuit model and the film resistivity ($\bar{\rho}_{xx}$) [see Fig. 2(a)]. We take the average value of the two devices measured for a given composition x . The resistivity of the 1 nm-thick Ta seed layer is assumed to be 200 $\mu\Omega\text{cm}$ [27].

B. MOKE signal

In Fig. 6(a), we show a line profile of light reflectivity along the wire width (orthogonal to the current flow) for $\text{Bi}_{1-x}\text{Sb}_x$ with $x = 0$. The corresponding MOKE

TABLE III. Average resistivity of $\text{Bi}_{1-x}\text{Sb}_x$ (ρ_{xx}) estimated from the parallel circuit model and the film resistivity ($\bar{\rho}_{xx}$).

x	ρ_{xx} ($\mu\Omega\text{ cm}$)
0	3913
0.12	1644
0.20	910
0.28	1237

signals (θ_K and η_K) are shown in Fig. 6(b). We find negligible contribution from the out of plane spin magnetic moment induced by the Oersted field, likely due to the small current passed along the wire.

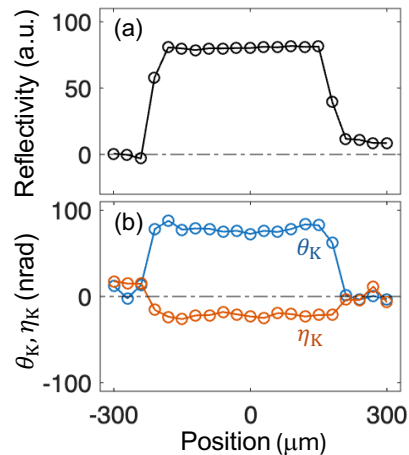


FIG. 6. (a,b) Line profile of the reflectivity (a) and θ_K and η_K (b) along the wire width (orthogonal to the current flow) for $\text{Bi}_{1-x}\text{Sb}_x$ with $x = 0$.

θ_K/j and η_K/j are plotted against the Sb concentration x in Figs. 7(a) and 7(b), respectively, using open circles. Both θ_K/j and η_K/j decrease with increasing x . The x dependence of $|\theta_K + i\eta_K|/j$ is plotted in Fig. 7(c): the data (open circles) are the same with those presented in Fig. 4(a).

C. Model calculations

Here, we show the calculation results when contribution from the orbital Hall effect on the MOKE signal is included. Following the approach described in Ref. [5], θ_K and η_K are expressed as the following:

$$\theta_K + i\eta_K \sim \langle (\varepsilon_{zx}^s + \varepsilon_{zx}^o) g(\varepsilon_{xx}, \theta) \rangle. \quad (8)$$

$g(\varepsilon_{xx}, \theta)$ represents factors related to the reflection of light from the film under an oblique incidence. $\langle X \rangle$ indicates X integrated along the film thickness. The off-diagonal component of the permittivity tensor $\varepsilon_{zx}^{s[0]}$ is cal-

culated using the following relation[5]:

$$\varepsilon_{zx}^{s[o]} = \frac{i}{\varepsilon_0 \omega} \frac{n_{s[o]}}{D_F} \left. \frac{\partial \sigma_{s[o]}(\omega)}{\partial E} \right|_{E_F} \quad (9)$$

where the spin [orbital] accumulation $n_{s[o]}$ is obtained by solving the spin [orbital] diffusion equation and reads

$$n_{s[o]} = -e D_F l_{s[o]} \sigma_{s[o]}(0) \rho_{xx}^2 j_x \frac{\sinh\left(\frac{t-2z}{2l_{s[o]}}\right)}{\cosh\left(\frac{t}{2l_{s[o]}}\right)}. \quad (10)$$

$\sigma_{s[o]}(0)$ and $l_{s[o]}$ are the dc spin [orbital] Hall conductivity and the associated diffusion length, respectively. $\sigma_{s[o]}(\omega)$ is the ac spin [orbital] Hall conductivity driven by the light electric field with angular frequency ω . $\left. \frac{\partial \sigma_{s[o]}(\omega)}{\partial E} \right|_{E_F}$ is the energy derivative of $\sigma_{s[o]}(\omega)$ evaluated at the Fermi energy. D_F is the density of states at the Fermi energy. z is a coordinate within the film, where $z = 0$ and $z = t$ corresponds to the bottom and top surfaces of the film that face the substrate and air, respectively.

The Maxwell's equations are solved numerically to compute the thickness averaged value of $\theta_K + i\eta_K$ [5, 28–30]. When solving the equations, material parameters are predefined as the following. The dc and ac spin [orbital] Hall conductivities ($\sigma_{s[o]}(0)$ and $\left. \frac{\partial \sigma_{s[o]}(\omega)}{\partial E} \right|_{E_F}$) are determined using the Kubo formula. We use a tight binding model to calculate the electronic state of $\text{Bi}_{1-x}\text{Sb}_x$ [22, 31, 32]. The Kubo formula reads

$$\sigma_{ji}^k(\omega) = i\hbar^2 e \sum_{\mathbf{k}, n, m} \frac{f(\epsilon_n) - f(\epsilon_m)}{\epsilon_n - \epsilon_m} \frac{\langle u_n | \hat{v}_j^k | u_m \rangle \langle u_m | \hat{v}_i | u_n \rangle}{\epsilon_n - \epsilon_m + \hbar\omega + i\eta}. \quad (11)$$

where \hat{v}_i is the i th component of the velocity operator, \hat{v}_j^k is the j th component of the spin (or orbital) current operator with spin (or orbital) direction along k . $|u_n\rangle$ is the Bloch eigenstate of an electron in band n (with wave vector \mathbf{k}) and ϵ_n is the corresponding eigenvalue. $f(\epsilon)$ is the Fermi-Dirac distribution function and η is a relaxation constant. Here we use $\eta = 25$ meV and the temperature inside the Fermi distribution function is room temperature. We employed a k -mesh with dimensions of $11 \times 11 \times 11$ to sample the irreducible Brillouin zone. In the main text, we use $\sigma_{s[o]}(\omega) = \sigma_{zx}^y(\omega)$, where the spin [orbital] magnetic moment points along y . $\sigma_{ij}^k(\omega)$ reduces to $\sigma_{ij}^k(0)$ in the limit of $\omega \rightarrow 0$.

The x -dependence of $\sigma_{s[o]}(0)$ and $\left. \frac{\partial \sigma_{s[o]}(\omega)}{\partial E} \right|_{E_F}$ are shown in Fig. 7(d-f). As is evident, $\sigma_s(0)$ is nearly constant in the range of x shown here, consistent with previous calculations[32]. $\sigma_o(0)$, on the other hand, tends to decrease with increasing x . The magnitude of $\sigma_o(0)$ is nearly one third of $\sigma_s(0)$ when $x = 0$, in agreement with a previous report on Bi[22]. Variation of $\left. \frac{\partial \sigma_{s[o]}(\omega)}{\partial E} \right|_{E_F}$ with x is somewhat larger for the orbital component than that of the spin counterpart. Note that the magnitude of $\left. \frac{\partial \sigma_{s[o]}(\omega)}{\partial E} \right|_{E_F}$ of $\text{Bi}_{1-x}\text{Sb}_x$ is more than one order of magnitude smaller than that of the transition metals[5].

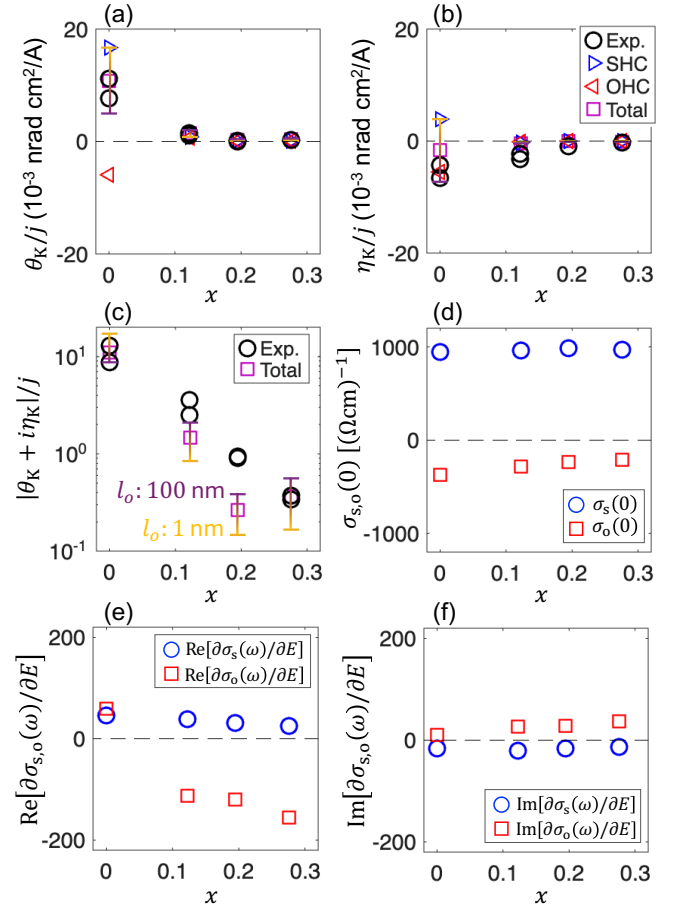


FIG. 7. Sb concentration x dependence of the real part θ_K (a), the imaginary part η_K (b) and the magnitude $|\theta_K + i\eta_K|$ (c) of current induced MOKE signal normalized by the current density j . Black circles represent experimental data. Data from two devices on the same substrates are presented. Blue and red triangles and purple squares show contributions from the spin Hall effect, the orbital Hall effect and the sum of the two, respectively. The symbols show results when $l_s = l_o = 18$ nm for all x . The yellow and purple error bars attached to the squares in (a-c) indicate the calculated MOKE signal when l_o is set to 1 nm and 100 nm, respectively. The unit of the y -axis of (c) is 10^{-3} nrad cm^2/A . (d) Sb concentration x dependence of dc spin Hall conductivity $\sigma_{SH}(0)$ and dc orbital Hall conductivity $\sigma_{OH}(0)$. (e,f) Real (e) and imaginary (f) parts of $\left. \frac{\partial \sigma_{s[o]}(\omega)}{\partial E} \right|_{E_F}$ plotted against x . The unit of the y -axis of (e,f) is $(\Omega \text{ cm eV})^{-1}$.

ε_{xx} of $\text{Bi}_{1-x}\text{Sb}_x$ is determined by the refractive index n and the extinction coefficient k , obtained using standard ellipsometry measurements. The x dependence of n and k are shown in Fig. 2(d). ε_{xx} of the SiO_2 substrate is set to $n = 1.5, k = 0$. We use $n = 1, k = 0$ for air and neglect the capping layer (1 nm thick oxidized Ti) for simplicity. ρ_{xx} is obtained from Table III. l_s for Bi (~ 18 nm) was determined previously using transport measurements[33]. Here we fix l_s and l_o to 18 nm for all

x .

The calculated MOKE signal is shown in Fig. 7(a-c). The right and left pointing triangles in Fig. 7(a,b) show the x dependence of the calculated MOKE signals (θ_K/j , η_K/j) when contribution from the spin and orbital Hall effects are considered, respectively. The squares represent the sum of the two contributions. For $x = 0$, the spin and orbital Hall effects tend to cancel out each other due to the difference in sign of $\sigma_{SH}(0) \frac{\partial \sigma_{SH}(\omega)}{\partial E}$ and $\sigma_{OH}(0) \frac{\partial \sigma_{OH}(\omega)}{\partial E}$, similar to the case in Pt[5]. In contrast,

the two effects add up for $x > 0$. The magnitude of the MOKE signal, $|\theta_K + i\eta_K|/j$, is plotted against x in Fig. 7(c). The colored error bars attached to the squares show the range of θ_K and η_K when l_o is varied: the yellow and purple horizontal bars indicate the corresponding limits when $l_o = 1$ nm and $l_o = 100$ nm, respectively. The calculated results roughly agrees with the experiments for $x = 0$ and $x \sim 0.28$ but are smaller when $x \sim 0.12$ and 0.2 . It is possible that contribution from the topological surface states, which is neglected in the model calculations, may influence the experimental results.

-
- [1] Y. K. Kato, R. C. Myers, A. C. Gossard, and D. D. Awschalom, Observation of the spin Hall effect in semiconductors, *Science* **306**, 1910 (2004).
- [2] O. M. J. van't Erve, A. T. Hanbicki, K. M. McCreary, C. H. Li, and B. T. Jonker, Optical detection of spin Hall effect in metals, *Appl. Phys. Lett.* **104**, 172402 (2014).
- [3] C. Stamm, C. Murer, M. Berritta, J. Feng, M. Gabureac, P. M. Oppeneer, and P. Gambardella, Magneto-Optical Detection of the Spin Hall Effect in Pt and W Thin Films, *Phys. Rev. Lett.* **119**, 087203 (2017).
- [4] T. Yokouchi and Y. Shiomi, Enhancement of Current-Induced Out-of-Plane Spin Polarization by Heavy-Metal-Impurity Doping in Fe Thin Films, *Physical Review Applied* **16**, 054001 (2021).
- [5] Y. Marui, M. Kawaguchi, S. Sumi, H. Awano, K. Nakamura, and M. Hayashi, Spin and orbital Hall currents detected via current-induced magneto-optical Kerr effect in V and Pt, *Phys. Rev. B* **108**, 144436 (2023).
- [6] P. Riego, S. Velez, J. M. Gomez-Perez, J. A. Arregi, L. E. Hueso, F. Casanova, and A. Berger, Absence of detectable current-induced magneto-optical Kerr effects in Pt, Ta, and W, *Appl. Phys. Lett.* **109**, 172402 (2016).
- [7] Y. D. Su, H. Wang, J. Li, C. S. Tian, R. Q. Wu, X. F. Jin, and Y. R. Shen, Absence of detectable MOKE signals from spin Hall effect in metals, *Appl. Phys. Lett.* **110**, 042401 (2017).
- [8] Y. G. Choi, D. Jo, K. H. Ko, D. Go, K. H. Kim, H. G. Park, C. Kim, B. C. Min, G. M. Choi, and H. W. Lee, Observation of the orbital Hall effect in a light metal Ti, *Nature* **619**, 52 (2023).
- [9] T. Tanaka, H. Kontani, M. Naito, T. Naito, D. S. Hirashima, K. Yamada, and J. Inoue, Intrinsic spin Hall effect and orbital Hall effect in 4d and 5d transition metals, *Phys. Rev. B* **77**, 165117 (2008).
- [10] H. Kontani, T. Tanaka, D. S. Hirashima, K. Yamada, and J. Inoue, Giant Orbital Hall Effect in Transition Metals: Origin of Large Spin and Anomalous Hall Effects, *Phys. Rev. Lett.* **102**, 016601 (2009).
- [11] D. Go, D. Jo, C. Kim, and H. W. Lee, Intrinsic Spin and Orbital Hall Effects from Orbital Texture, *Phys. Rev. Lett.* **121**, 086602 (2018).
- [12] D. Jo, D. Go, and H. W. Lee, Gigantic intrinsic orbital Hall effects in weakly spin-orbit coupled metals, *Phys. Rev. B* **98**, 214405 (2018).
- [13] L. Salemi and P. M. Oppeneer, First-principles theory of intrinsic spin and orbital Hall and Nernst effects in metallic monoatomic crystals, *Phys. Rev. Mater.* **6**, 095001 (2022).
- [14] I. Lyalin, S. Alikhah, M. Berritta, P. M. Oppeneer, and R. K. Kawakami, Magneto-Optical Detection of the Orbital Hall Effect in Chromium, *Phys. Rev. Lett.* **131**, 156702 (2023).
- [15] D. Hsieh, D. Qian, L. Wray, Y. Xia, Y. S. Hor, R. J. Cava, and M. Z. Hasan, A topological Dirac insulator in a quantum spin Hall phase, *Nature* **452**, 970 (2008).
- [16] J. C. Y. Teo, L. Fu, and C. L. Kane, Surface states and topological invariants in three-dimensional topological insulators: Application to $\text{Bi}_{1-x}\text{Sb}_x$, *Phys. Rev. B* **78**, 045426 (2008).
- [17] H. J. Zhang, C. X. Liu, X. L. Qi, X. Dai, Z. Fang, and S. C. Zhang, Topological insulators in Bi_2Se_3 , Bi_2Te_3 and Sb_2Te_3 with a single Dirac cone on the surface, *Nat. Phys.* **5**, 438 (2009).
- [18] N. H. D. Khang, Y. Ueda, and P. N. Hai, A conductive topological insulator with large spin Hall effect for ultralow power spin-orbit torque switching, *Nat. Mater.* **17**, 808 (2018).
- [19] Y. Fuseya, M. Ogata, and H. Fukuyama, Spin-Hall Effect and Diamagnetism of Dirac Electrons, *J. Phys. Soc. Jpn.* **81**, 093704 (2012).
- [20] Y. Fuseya, M. Ogata, and H. Fukuyama, Transport Properties and Diamagnetism of Dirac Electrons in Bismuth, *J. Phys. Soc. Jpn.* **84**, 012001 (2015).
- [21] Z. Chi, G. Qu, Y.-C. Lau, M. Kawaguchi, J. Fujimoto, K. Takanashi, M. Ogata, and M. Hayashi, Spin Hall effect driven by the spin magnetic moment current in Dirac materials, *Phys. Rev. B* **105**, 214419 (2022).
- [22] G. Qu and G. Tatara, Intrinsic orbital and spin Hall effect in bismuth semimetal, *Phys. Rev. B* **107**, 214421 (2023).
- [23] Z. Chi, Y.-C. Lau, X. Xu, T. Ohkubo, K. Hono, and M. Hayashi, The spin Hall effect of Bi-Sb alloys driven by thermally excited Dirac-like electrons, *Science Advances* **6**, eaay2324 (2020).
- [24] S. Zhang, H. Pi, Z. Fang, H. Weng, and Q. Wu, New perspectives of Hall effects from first principles calculations, *arXiv:2401.15150* (2024).
- [25] J. A. van Hulst, H. M. Jaeger, and S. Radelaar, Epitaxial growth of bismuth films and bismuth-antimony heterostructures, *Phys. Rev. B* **52**, 5953 (1995).
- [26] B. Lenoir, M. Cassart, J. P. Michenaud, H. Scherrer, and S. Scherrer, Transport properties of Bi-rich Bi-Sb alloys, *J. Phys. Chem. Solids* **57**, 89 (1996).
- [27] J. Kim, P. Sheng, S. Takahashi, S. Mitani, and M. Hayashi, Spin hall magnetoresistance in metallic bi-

- layers, *Phys. Rev. Lett.* **116**, 097201 (2016).
- [28] P. Yeh, Optics of anisotropic layered media: A new 4×4 matrix algebra, *Surface Science* **96**, 41 (1980).
- [29] S. Visnovsky, Magneto-optical ellipsometry, *Czechoslovak Journal of Physics B* **36**, 625 (1986).
- [30] J. Zak, E. R. Moog, C. Liu, and S. D. Bader, Universal approach to magneto-optics, *J. Magn. Magn. Mater.* **89**, 107 (1990).
- [31] Y. Liu and R. E. Allen, Electronic-structure of the semimetals Bi and Sb, *Phys. Rev. B* **52**, 1566 (1995).
- [32] C. Sahin and M. E. Flatte, Tunable Giant Spin Hall Conductivities in a Strong Spin-Orbit Semimetal: $\text{Bi}_{1-x}\text{Sb}_x$, *Phys. Rev. Lett.* **114**, 107201 (2015).
- [33] H. Hirose, M. Kawaguchi, Y. C. Lau, Z. D. Chi, F. Freimuth, K. Takanashi, and M. Hayashi, Interface-enhanced helicity dependent photocurrent in metal/semimetal bilayers, *Phys. Rev. B* **103**, 174437 (2021).
- [34] S. D. Sarma and E. H. Hwang, Universal density scaling of disorder-limited low-temperature conductivity in high-mobility two-dimensional systems, *Phys. Rev. B* **88**, 035439 (2013).
- [35] S. D. Sarma, E. H. Hwang, and H. Min, Carrier screening, transport, and relaxation in three-dimensional Dirac semimetals, *Phys. Rev. B* **91**, 035201 (2015).
- [36] H. M. Benia, C. Strasser, K. Kern, and C. R. Ast, Surface band structure of $\text{Bi}_{1-x}\text{Sb}_x(111)$, *Phys. Rev. B* **91**, 161406 (2015).
- [37] L. Baringthon, T. H. Dang, H. Jaffres, N. Reyren, J. M. George, M. Morassi, G. Patriarche, A. Lemaitre, F. Bertran, and P. L. Fevre, Topological surface states in ultrathin $\text{Bi}_{1-x}\text{Sb}_x$ layers, *Phys. Rev. Mater.* **6**, 074204 (2022).
- [38] A. A. Burkov and L. Balents, Weyl Semimetal in a Topological Insulator Multilayer, *Phys. Rev. Lett.* **107**, 127205 (2011).
- [39] L. Vila, T. Kimura, and Y. Otani, Evolution of the spin hall effect in Pt nanowires: Size and temperature effects, *Phys. Rev. Lett.* **99**, 226604 (2007).
- [40] J. Sinova, S. O. Valenzuela, J. Wunderlich, C. H. Back, and T. Jungwirth, Spin Hall effects, *Rev. Mod. Phys.* **87**, 1213 (2015).
- [41] S. Y. Peng, X. Zheng, S. Li, B. Lao, Y. M. Han, Z. L. Liao, H. S. Zheng, Y. M. Yang, T. Y. Yu, P. T. Liu, Y. Sun, X. Q. Chen, S. Z. Peng, W. S. Zhao, R. W. Li, and Z. M. Wang, Unconventional scaling of the orbital Hall effect, *Nat. Mater.* **24**, 1749 (2025).
- [42] L. Li, J. G. Checkelsky, Y. S. Hor, C. Uher, A. F. Hebard, R. J. Cava, and N. P. Ong, Phase transitions of Dirac electrons in bismuth, *Science* **321**, 547 (2008).
- [43] Z. W. Zhu, B. Fauque, Y. Fuseya, and K. Behnia, Angle-resolved Landau spectrum of electrons and holes in bismuth, *Phys. Rev. B* **84**, 115137 (2011).
- [44] Y. Fukushima, K. Kawaguchi, K. Kuroda, M. Ochi, M. Hirayama, R. Mori, H. Tanaka, A. Harasawa, T. Iimori, Z. G. Zhao, S. Tani, K. Yaji, S. Shin, F. Komori, Y. Kobayashi, and T. Kondo, Spin-polarized saddle points in the topological surface states of elemental bismuth revealed by pump-probe spin- and angle-resolved photoemission spectroscopy, *Phys. Rev. B* **110**, L041401 (2024).
- [45] E. J. Konig, I. M. Dzero, A. Levchenko, and D. A. Pesin, Gyrotropic Hall effect in Berry-curved materials, *Phys. Rev. B* **99**, 155404 (2019).
- [46] F. Mahfouzi, M. D. Stiles, and P. M. Haney, Current-induced circular dichroism on metallic surfaces: A first-principles study, *Phys. Rev. B* **111**, 014415 (2025).
- [47] F. Mahfouzi, M. D. Stiles, and P. M. Haney, Electric field-induced Kerr rotation on metallic surfaces, *Phys. Rev. B* **112**, 195428 (2025).
- [48] M. Tanabe, R. Okukawa, T. Yokouchi, Y. Miyata, and Y. Shiomi, Pockels effect in CVD-grown monolayer MoS_2 , *Japanese Journal of Applied Physics* **64**, 055002 (2025).
- [49] D. G. Ovalle, A. Pezo, and A. Manchon, Orbital Kerr effect and terahertz detection via the nonlinear Hall effect, *Phys. Rev. B* **110**, 094439 (2024).